Monthly Notices of the ROYAL ASTRONOMICAL SOCIETY

MNRAS **462,** S312–S322 (2016) doi:10.1093/mnras/stw2942
Advance Access publication 2016 November 17

Statistical analysis of suprathermal electron drivers at 67P/Churyumov–Gerasimenko

Thomas W. Broiles,[1★] J. L. Burch,[1] K. Chae,[1] G. Clark,[2★] T. E. Cravens,[3] A. Eriksson,[4] S. A. Fuselier,[1,5] R. A. Frahm,[1] S. Gasc,[6] R. Goldstein,[1] P. Henri,[7] C. Koenders,[8] G. Livadiotis,[1★] K. E. Mandt,[1,5] P. Mokashi,[1] Z. Nemeth,[9] E. Odelstad,[4] M. Rubin[6] and M. Samara[10]

[1]*Division of Space Science and Engineering, Southwest Research Institute, 6220 Culebra Road, San Antonio, TX 78238, USA*
[2]*The Johns Hopkins University Applied Physics Laboratory, 11100 Johns Hopkins Road, Laurel, MD 20723, USA*
[3]*Department of Physics and Astronomy, University of Kansas, 1450 Jayhawk Boulevard, Lawrence, KS 66045, USA*
[4]*Swedish Institute of Space Physics, Box 537, SE-751 21 Uppsala, Sweden*
[5]*Department of Physics and Astronomy, The University of Texas at San Antonio, San Antonio, TX 78249, USA*
[6]*Physikalisches Institut, University of Bern, Sidlerstrasse 5, CH-3012 Bern, Switzerland*
[7]*Centre National de la Recherche Scientifique, LPC2E, CNRS, F-45071 Orléans, France*
[8]*Institut für Geophysik und extraterrestrische Physik, Technische Universität Braunschweig, Mendelssohnstraße 3, D-38106 Braunschweig, Germany*
[9]*Wigner Research Centre for Physics, 1121 Budapest, Hungary*
[10]*Heliophysics Division, Goddard Space Flight Center, 8800 Greenbelt Road, Greenbelt, MD 20771, USA*

Accepted 2016 November 11. Received 2016 November 9; in original form 2016 May 26

ABSTRACT

We use observations from the Ion and Electron Sensor (IES) on board the *Rosetta* spacecraft to study the relationship between the cometary suprathermal electrons and the drivers that affect their density and temperature. We fit the IES electron observations with the summation of two kappa distributions, which we characterize as a dense and warm population ($\sim$10 cm^{-3} and $\sim$16 eV) and a rarefied and hot population ($\sim$0.01 cm^{-3} and $\sim$43 eV). The parameters of our fitting technique determine the populations' density, temperature, and invariant kappa index. We focus our analysis on the warm population to determine its origin by comparing the density and temperature with the neutral density and magnetic field strength. We find that the warm electron population is actually two separate sub-populations: electron distributions with temperatures above 8.6 eV and electron distributions with temperatures below 8.6 eV. The two sub-populations have different relationships between their density and temperature. Moreover, the two sub-populations are affected by different drivers. The hotter sub-population temperature is strongly correlated with neutral density, while the cooler sub-population is unaffected by neutral density and is only weakly correlated with magnetic field strength. We suggest that the population with temperatures above 8.6 eV is being heated by lower hybrid waves driven by counterstreaming solar wind protons and newly formed, cometary ions created in localized, dense neutral streams. To the best of our knowledge, this represents the first observations of cometary electrons heated through wave–particle interactions.

Key words: magnetic fields – plasmas – waves – methods: data analysis – solar wind – comets: individual: 67P/Chuyumov–Gerasimenko.

1 INTRODUCTION

Comets produce neutral gas through the sublimation of water, carbon dioxide, and other trace elements. The neutral gas forms an exosphere also known as a coma. Gas in the coma moves radially away from the nucleus, and a substantial fraction is eventually ionized through photoionization from solar ultraviolet radiation, charge exchange with the solar wind, or electron impact ionization (Cravens 1987; Cravens et al. 1987; Gan & Cravens 1990). *In situ* observations of cometary ionospheres have been made at comets 1P/Halley (Gringauz et al. 1986; Johnstone 1990; Larson et al. 1992), Giacobini–Zinner (Bame et al. 1986; Thomsen

★ E-mail: tbroiles@spacescience.org (TWB); george.clark@jhuapl.edu (GC); glivadiotis@swri.edu (GL)

et al. 1986; Zwickl et al. 1986), Grigg–Skjellerup (Reme et al. 1993), 19P/Borrelly (Nordholt et al. 2003; Young et al. 2004), and recently at 67P/Churyumov–Gerasimenko (67P) (Broiles et al. 2015; Burch et al. 2015; Clark et al. 2015; Edberg et al. 2015; Goldstein et al. 2015; Nilsson et al. 2015a; Behar et al. 2016).

Observations of cometary electrons have been made at all the comets mentioned above, but we especially highlight the *International Cometary Explorer*'s flyby of Giacobini–Zinner. Bame et al. (1986) performed a moment analysis of the electron environment throughout the closest approach and found that a number of distinct regions could be classified by the electron properties. Zwickl et al. (1986) used the same data and refined the analysis by characterizing the electrons into cold ($T \approx 2$ eV), mid ($T \approx 10$ eV), and hot ($T \approx 20$ eV) populations and fitted each with Maxwellian distributions. Both Bame et al. (1986) and Zwickl et al. (1986) found that the electron temperature was hottest in the flanks of the coma, far from the nucleus.

Edberg et al. (2015) studied the bulk electron environment at 67P. They infer the bulk electron density with *Rosetta's* Langmuir Probe (LAP) and Mutual Impedance Probe (MIP) (Eriksson et al. 2006; Trotignon et al. 2006). They found that the bulk electron density is inversely proportional to the distance from the comet, and that the bulk electron density is proportional to the local neutral density enhancements (Hässig et al. 2015).

Clark et al. (2015) performed the first study of cometary suprathermal electrons at 67P by fitting the electrons below a few hundred eV with a flattop distribution (Thomsen et al. 1986). Flattop distributions are known to form in electron populations that have passed through a shock, and through wave–particle interactions. However, a shock was unlikely to have formed at 67P when it was more than 3 au from the Sun. Consequently, Clark et al. (2015) concluded that the electrons must be heated by waves, and speculated that lower hybrid waves were a likely candidate.

Broiles et al. (2016) extended this study of the cometary electron environment at 67P by performing case studies when it was far from the Sun (∼3 au), and near perihelion (∼1.3 au). They also found that the velocity space density of cometary electrons was well fitted by the summation of two kappa functions. Broiles et al. (2016) characterized the two kappa functions as a warm and dense population, and a hot and rarefied population. They concluded that they were observing the mid and hot populations described by Zwickl et al. (1986) for the flyby of Giacobini–Zinner. They also determined that the hot population was likely the solar wind halo electrons penetrating the coma along the interplanetary magnetic field, but they were unable to determine the origin of the warm population.

In this work, we attempt to determine the origin of the warm electron population described by Broiles et al. (2016) using statistical analysis of the warm electron population, neutral gas, and magnetic field surrounding comet 67P/Churyumov–Gerasimenko. We rely on the same fitting and instrument calibration techniques as defined by Broiles et al. (2016) to infer the physical parameters of the warm electron population on 2014 November 1. We then compare the warm electron density and temperature with the magnetic field strength and neutral gas density at *Rosetta*. Finally, we qualitatively compare the warm electron temperature with the spectrum of electrostatic fluctuations. We expect to find relationships between the different drivers and the warm electron population, which may indicate its origin.

2 INSTRUMENTATION

The IES is a plasma spectrometer on board *Rosetta* and is a member of the Rosetta Plasma Consortium (Burch et al. 2007; Carr et al. 2007). The IES counts ions and electrons with a pair of stacked, toroidal electrostatic analysers from 4.3 eV q^{-1} to 18 keV q^{-1} with 8 per cent $\Delta E/E$ energy resolution. The instrument has a 360 × 90-deg^2 field of view with an azimuthal resolution of 22°.5 for the electron sensor and 45° for the ion sensor, and an elevation resolution of 6° for both. We note that one 45° segment of the ion sensor has a fine azimuthal resolution of 5°. Measurement cycles have a variable cadence ranging from 128 to 1024 s.

Telemetry constraints prohibit the IES from returning all of the measured data to the Earth. Consequently, the IES relies on measurement modes to reduce the size of its data product by summing adjacent measurements in azimuth, elevation, or energy to meet specific science goals.

In order to convert measurements of raw counts into physical units, we rely on a geometric factor characterized through laboratory testing prior to the launch of *Rosetta* (Burch et al. 2007). However, Broiles et al. (2016) found that laboratory testing could not account for all possible distortions, including spacecraft blockages, differential sensitivity between detectors, or the ageing of spacecraft components in flight. They developed a new version of the geometric factor for the electron sensor based observations made in flight, which assumes that the electron distribution is isotropic. We rely on the flight calibrated version of the geometric factor in this work, and it is publicly available on the European Space Agency's (ESA) Planetary Science Archive.

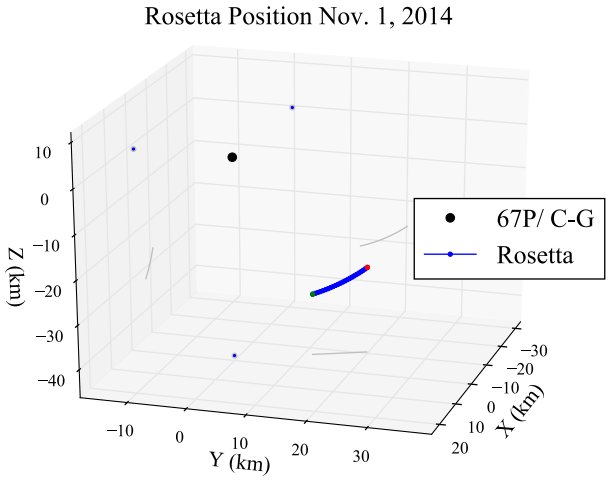

Figure 1. A schematic of the *Rosetta* position relative to 67P on 2014 November 1 in CSEQ coordinates. Projections of the comet and flyby in the *X*–*Y*, *Y*–*Z*, and *X*–*Z* planes are shown in grey in the background. The green and red points, respectively, mark the start and end of the day.

3 OBSERVATIONS

Fig. 1 shows the position of *Rosetta* relative to 67P between 00:00 on 2014 November 1. (green dot) and 00:00 2014 November 2 (red dot) in Comet–Sun–Equatorial (CSEQ) coordinates. The CSEQ frame is cometocentric, with the $+X$ direction pointing from the comet to the Sun, the $+Z$ direction is the component of the Sun's north pole of date orthogonal to $+X$, and the $+Y$ direction is orthogonal to both $+X$ and $+Z$. Two-dimensional projections of spacecraft and comet position for the *X*–*Y*, *X*–*Z*, and *Y*–*Z* planes are shown in the background as grey lines. *Rosetta* was in the Southern hemisphere of the coma, slightly anti-Sunward of the terminator plane, and ∼25 km from the nucleus throughout the day. *Rosetta* moved very little relative to the comet throughout the day compared to the

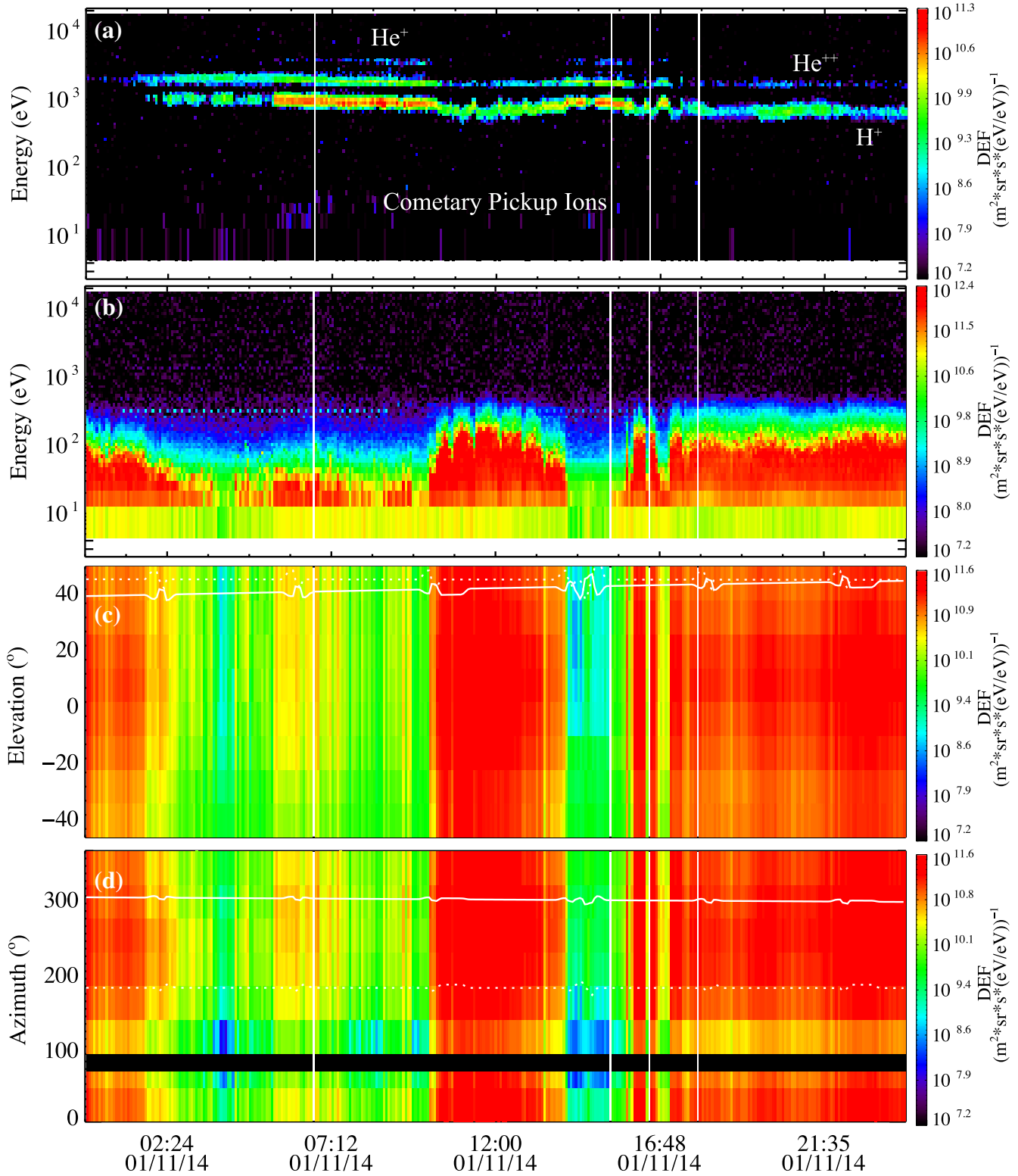

Figure 2. IES ion and electron DEF between 00:00 2014 November 1 and 00:00 2014 November 2. Panels (a) and (b) show the DEF averaged over azimuths and elevations for each energy step over time for ions and electrons, respectively. Panel (c) shows the DEF averaged over energy and azimuth for each elevation step over time. Panel (d) shows the DEF averaged over elevation and energy for each azimuth over time. The solid and dashed lines in panels (c) and (d), respectively, represent the position of the Sun and 67P in the IES's field of view.

~1000 km gyroradius of cometary pickup ions in 1 keV solar wind with 10 nT magnetic field.

Fig. 2 shows spectrograms of IES ion and electron observations in the form of differential energy flux (DEF) from 00:00 2014 November 01 to 00:00 2014 November 02. Fig. 2(a) contains IES ion DEF averaged over azimuth and elevation for each energy step versus time. Fig. 2(b) contains IES electron DEF averaged over elevation and azimuth for each energy step versus time. Fig. 2(c)

contains IES electron DEF averaged over energy and azimuth for each elevation versus time. Fig. 2(d) contains IES electron DEF averaged over energy and elevation for each azimuth versus time. The location of the Sun and 67P in the IES's field of view is shown by white solid and dashed lines, respectively. Solid white vertical lines are individual measurement cycles where no data were returned and do not highlight time intervals of interest. We note that the colour of each spectrogram ranges from the lower detection limit of the instrument to the peak DEF for that specific dimension in the observed time range. Allowing the colour to span the full detectable range of the instrument shows absolute signal strength rather than highlighting small relative differences.

The IES ion observations are qualitatively similar to an inactive comet shown by Goldstein et al. (2015), Nilsson et al. (2015a), and Broiles et al. (2015). Fig. 2(a) shows that a strong signal is present at 700 eV q^{-1} along with a strongly correlated signal at 1400 eV q^{-1}, and another at 2800 eV q^{-1}. The first two signals are solar wind H^+ and He^{++}, while the highest energy signal is He^+ that has gained an electron through charge exchange with cometary neutrals (Fuselier et al. 1991). Very recently created cometary ions are also faintly visible near 07:00 and 15:00 at energies below 50 eV (Nilsson et al. 2015a). Before 04:00, between 10:00 and 14:00, and after 17:00 the solar wind protons show substantial heating, deceleration, and, occasionally, disappear completely.

The electron DEF shown in Fig. 2(b) is highly variable below 100 eV throughout the day, which is qualitatively similar to observations shown by Clark et al. (2015) and Broiles et al. (2016). In particular, we note the high DEF present below 100 eV in the intervals from 00:00 to 04:00, 10:00 to 14:00, and 17:00 through the remainder of the day. The interval of high DEF between 10:00 and 14:00 contains periodic dips, which have a periodicity of 45 min to an hour. We note that periodic increases in DEF at narrow energy ranges between 200 and 2000 eV – visible as dotted, horizontal lines – are the result of interference from the Ion Composition Analyzer (ICA) (Nilsson et al. 2007).

The electron DEF is also relatively isotropic in Figs 2(c) and (d). There is a slight drop in DEF between azimuths 45° and 135°; however, this is likely to be caused by imperfections in the flight-calibrated geometric factor developed by Broiles et al. (2016), rather than a real anisotropy in the electrons. Nevertheless, data from azimuths 0° to 180° are excluded from our fitting analysis, and consequently this localized drop in DEF will not affect our results. Additionally, we note that the spacecraft remained at a relatively fixed attitude relative to 67P (panels c and d, dashed white line) and the Sun (panels c and d, solid white line) throughout the day with the exception of nine changes in spacecraft attitude that occur every 3–4 h and have a duration of ∼25 min.

4 FITTING ANALYSIS

4.1 Fitting technique

We fit the electron observations using the same technique as described by Broiles et al. (2016), but we will briefly review our approach below. Each measured distribution of electrons with the summation of two kappa functions similar to that defined by equation (3.5) of Livadiotis & McComas (2013), and the version used in our fit, is shown in equation (1). The distribution function f is defined by the population's density, n, bulk velocity, $\langle \boldsymbol{v} \rangle$, temperature, T, invariant kappa index, κ_0, and spacecraft potential, ϕ_{SC}. We note that the constants are electron charge, q, electron mass, m_e, and

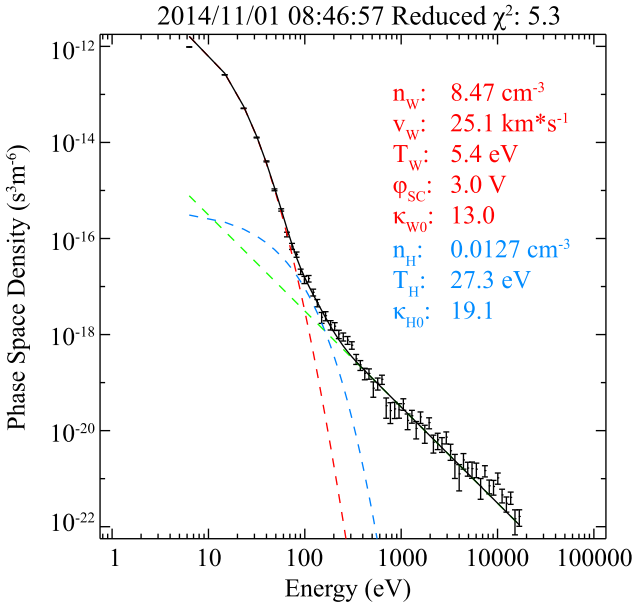

Figure 3. A case study of our fitting analysis for a single measurement that began on 2014 November 1 at 08:46:57. Black bars: observed phase space density; red dashed curve: warm population; blue dashed curve: hot population; green dashed line: assumed background of 1.2 counts s^{-1}; and solid black line: summation of the warm, hot, and background populations.

the Boltzmann constant, k. The two kappa functions are inferred to be separate populations: a warm, relatively dense population and a hot, rarefied population. Equation (1) is used to fit the warm and hot populations. However, in the case of the hot population, the bulk velocity and spacecraft potential are assumed to be negligibly small. The spacecraft potential is a fixed value that is determined by LAP (Eriksson et al. 2006; Odelstad et al. 2015).

$$f = \frac{n}{\kappa_0 \pi \left(\frac{2kT}{m_e}\right)} \frac{\Gamma\left(\kappa_0 + \frac{5}{2}\right)}{\Gamma\left(\kappa_0 + 1\right)} \times \left[1 + \frac{(v_x - \langle v_x \rangle)^2 + (v_y - \langle v_y \rangle)^2 + (v_z - \langle v_z \rangle)^2 + \frac{2q\phi_{SC}}{m_e}}{\kappa_0 \left(\frac{2kT}{m_e}\right)}\right]^{-\kappa_0 - \frac{5}{2}}. \quad (1)$$

As discussed in Section 3, measurements taken between azimuths 45° and 135° are anomalously low. This is a known instrumental effect, which is discussed in greater detail by Broiles et al. (2016), and gets significantly worse after 2015 April . We address this by excluding data with azimuths between 0° and 180° in our fit.

Fig. 3 shows an example of our fitting analysis for a single 256 s measurement starting at 08:46:57 on 2014 November 1. The fitting technique uses the full three-dimensional velocity space, but it is not possible to show the full three-dimensional fit. Consequently, we show the phase-space density at each energy step (black bars) summed over all elevations and azimuths between 180° and 360°. The observed phase-space density with uncertainty is shown by vertical black bars, while the fitted results for the warm and hot electron populations are represented by the red dashed curves and blue dashed curves, respectively. An assumed constant background level of 1.2 counts s^{-1} is also included and marked by the green dashed line. The summation of the warm, hot, and background distributions is represented by the solid black curve.

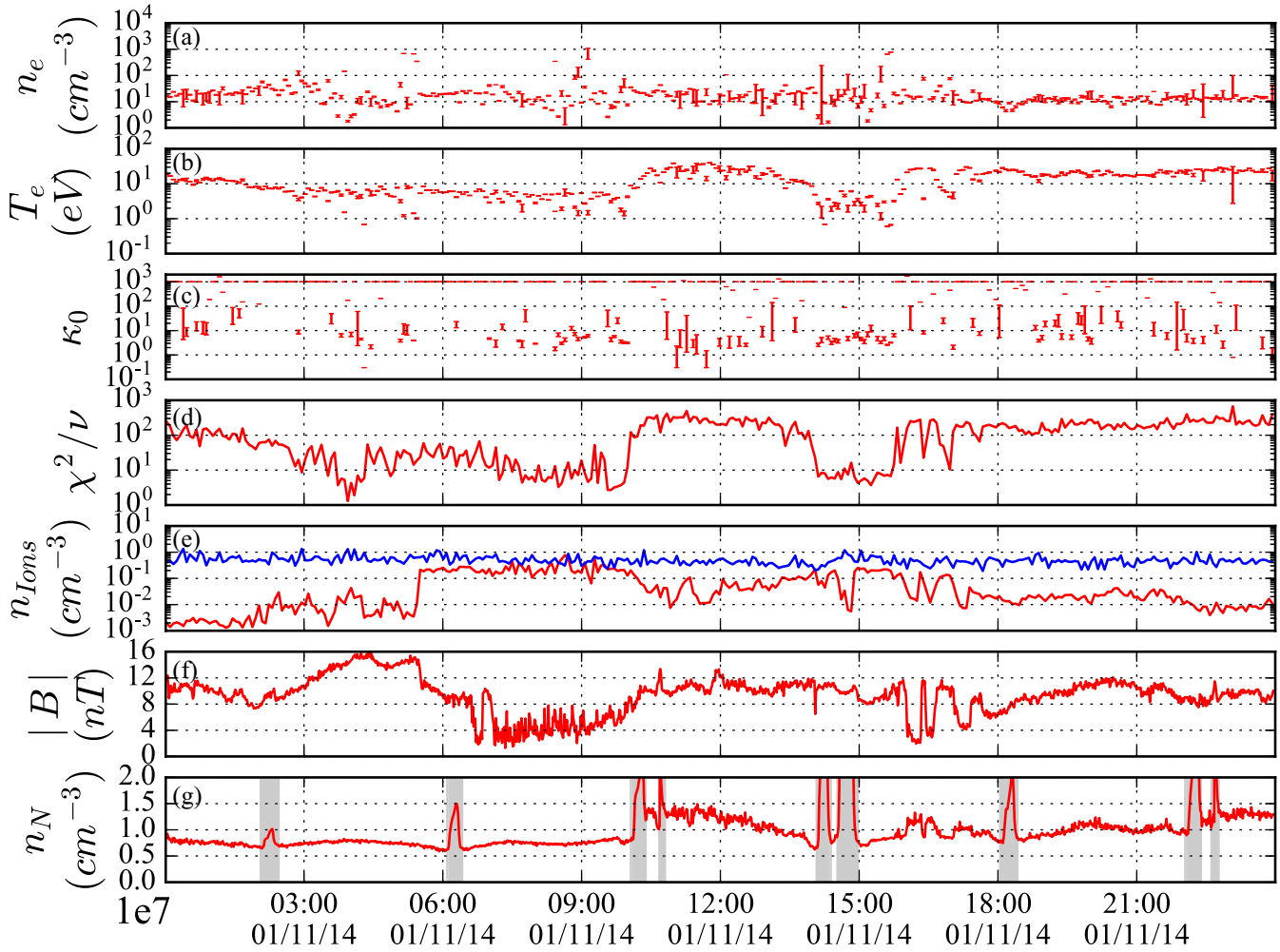

Figure 4. A time series of the fit results for the warm population along with RPC-Magnetometer and ROSINA-COPS observations on 2014 November 1. From the top to bottom: warm electron density, warm electron temperature, warm electron invariant kappa index, reduced χ^2 of the fit, cometary ion (blue) and solar wind proton (red) density, magnetic field strength, and neutral density. Uncertainty in our fit results is shown as vertical red bars. Vertical grey regions in panel g highlight the time intervals when COPS data were excluded from our analysis.

4.2 Time-series analysis

Fig. 4 shows the results of our fitting analysis, as a function of time, for the warm electron population observed by the IES on 2014 November 1 along with measurements from the RPC-Magnetometer and Rosetta Orbiter Spectrometer for Ion and Neutral Analysis-Cometary Pressure Sensor (ROSINA-COPS) (Balsiger et al. 2007; Glassmeier et al. 2007). From the top to bottom, Fig. 4 includes the warm electron density (panel a), warm electron temperature (panel b), warm electron invariant kappa index (panel c), the reduced χ^2 of the fitting analysis (panel d), the cometary ion and solar wind proton density computed from the zero-order moment of IES ion data (panel e), magnetic field strength (panel f), and neutral gas density (panel g). Uncertainties in the fit results are also included in panels (a)–(c). We note that the magnetometer team is still working to remove all spacecraft bias in their measurement, and consequently there may be an ∼2 nT offset in the magnetic field strength (Richter et al. 2015).

When compared with Fig. 2, we find that the increase in low-energy DEF observed before 02:00, between 10:00 and 14:00, and after 16:00 corresponds to a large increase in warm electron temperature (panel b). It is also interesting to note that the warm electron density (panel a) is typically in the range of 10–100 cm^{-3}, and does not appear to have the same behaviour as the warm electron temperature (panel b). We have visually checked the fitting results for the density measurements near 1000 cm^{-3} and found to be a poor fit. Consequently, we exclude the five or six measurements with densities above 250 cm^{-3} from further analysis. The invariant kappa index of the warm population (panel c) is similar to that observed by Broiles et al. (2016); κ_0 varies between 10 and 1000 and does so on time-scales shorter than an IES measurement cycle (i.e. 256 s on 2014 November 1). The reduced χ^2 of the fit (panel d) is closely correlated with the warm electron temperature. Broiles et al. (2016) noted the same result, but concluded it was likely the result of anisotropic heating. The magnetic field strength (panel f) is relatively enhanced from 02:00 to 06:00, 10:00 to 16:00, and 19:00 to the end of the day. The neutral gas density (panel g) has gradual changes intermixed with nine brief spikes in density. Given the relatively small motion of *Rosetta* relative to the comet, as shown in Fig. 1, the gradual changes in density are likely the result of enhanced neutral density regions that vary with the rotation of 67P (Hässig et al. 2015). The gradual variations in density are reasonably correlated with the warm electron temperature (panel b). In particular, we note the density enhancement starting at 10:00 and

Table 1. A list of time intervals on 2014 November 1 when spacecraft rotation occurred along with spikes in neutral density measured by COPS.

#	Start	Stop
1	2014 November 1 02:04	2014 November 1 02:27
2	2014 November 1 06:06	2014 November 1 06:25
3	2014 November 1 10:04	2014 November 1 10:23
4	2014 November 1 10:41	2014 November 1 10:48
5	2014 November 1 14:05	2014 November 1 14:23
6	2014 November 1 14:32	2014 November 1 14:58
7	2014 November 1 18:03	2014 November 1 18:25
8	2014 November 1 22:03	2014 November 1 22:23
9	2014 November 1 22:37	2014 November 1 22:46

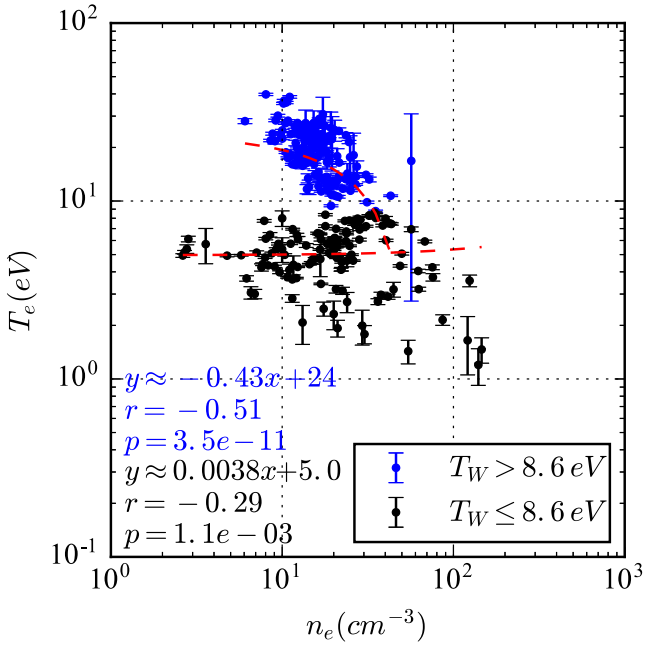

Figure 5. A scatter plot of the warm electron population's temperature versus density over the entire day of 2014 November 1. Measurements with a temperature above and below 8.6 eV are coloured blue and black, respectively. Linear regressions to both groups are shown as dashed red lines.

ending near 14:00, but there are others near the start and end of the day.

The brief spikes in neutral density in shaded grey regions are associated with nine spacecraft rotations, which are shown by the change in the position of the Sun and 67P in the IES's field of view in Figs 2(c) and (d). The spikes are likely caused by the sublimation of material off the spacecraft body from regions typically in darkness that are exposed to sunlight. The spacecraft rotations can increase the local neutral density around the spacecraft by an order of magnitude or more. Table 1 lists the nine time intervals associated with neutral density spikes, and are excluded from further analysis.

5 STATISTICAL ANALYSES WITH OTHER OBSERVATIONS

Fig. 5 shows the warm electron temperature as a function of warm electron density for all of the IES observations on 2014 November 1. Uncertainties in the fitting results are shown for the ordinate, which is used to weight the linear regression models shown by the dashed black and blue lines. We note that there is a clear break in the relationship of these two parameters near 30 cm^{-3} and 8.6 eV (100 000 K). Consequently, we divide our measurements into two separate sub-populations. The blue and black data represent fitting results with temperatures above and below 8.6 eV, respectively. We use this temperature paradigm to separate the observations for the remainder of the statistical analysis. For brevity, we refer to measurements above and below 8.6 eV as sub-populations 1 and 2, respectively. Both subsets of warm electrons have an inverse relationship between temperature and density, which are strongly correlated. However, population 1 (blue data) has a much higher temperature when the density is low and a steeper rate of cooling as the density increases.

Fig. 6 shows the warm electron density versus magnetic field strength (panel a) and warm electron temperature versus magnetic field strength for observations from 2014 November 1. Fit results for sub-population 1 are coloured blue, while fit results for sub-population 2 are coloured black. Measurements from the magnetometer are downsampled to have the same cadence as the IES so that the Pearson correlation could be performed. For each sub-population, the correlation, r, and the double-tailed statistical significance, p, are computed. Linear regression (red dashed line) is performed on a sub-population if the statistical significance of the correlation is less than 0.01. The correlation coefficient, statistical significance, and if relevant, the linear regression model are labelled in each panel for each sub-population using their respective colours. We find almost no correlation between density and magnetic field strength for either sub-population (panel a). A statistically significant relationship is present between the temperature and the magnetic field strength of sub-population 2 (panel b, black data), which has the relationship $T_W = 0.14 \times |\boldsymbol{B}| + 4.1$ eV, $|\boldsymbol{B}|$ in nT.

Fig. 7 shows the warm electron density versus the neutral density (panel a), the warm electron temperature versus neutral density (panel b), and the warm electron thermal pressure versus the neutral thermal pressure (panel c) for 2014 November 1. Results are shown in the same format as Fig. 6. No relationship exists between the warm electron density and the neutral density for either sub-population. In contrast, the temperature is strongly correlated with the neutral density for sub-population 1 ($r = 0.75$, $T_W = 2.4e-6 \times n_N - 6.7$ eV, n_N is in cm^{-3}). The warm electron thermal pressure is well correlated with the neutral thermal pressure (panel c) for sub-population 1 (i.e. $r = 0.63$, $P_e = 0.000\,92 \times P_N + 0.0061$, with P_e and P_N in nPa) but still weaker than the relationship between electron temperature and neutral density (panel b).

6 DISCUSSION

This study used data from *Rosetta*'s IES, RPC-Magnetometer, LAP, and COPS to determine drivers for cometary suprathermal electrons. Electron observations were fitted to the summation of two kappa distributions using the technique outlined by Broiles et al. (2016). We used observations from 2014 November 1 to correlate magnetic field strength and neutral density with the warm electron density and temperature.

Our analysis of IES fitting results, magnetic field, and neutral density on 2014 November 1 has resulted in the following:

(1) During three intervals on 2014 November 1, the electron DEF below 100 eV became very intense and correlated to a drop in the bulk energy of the solar wind.

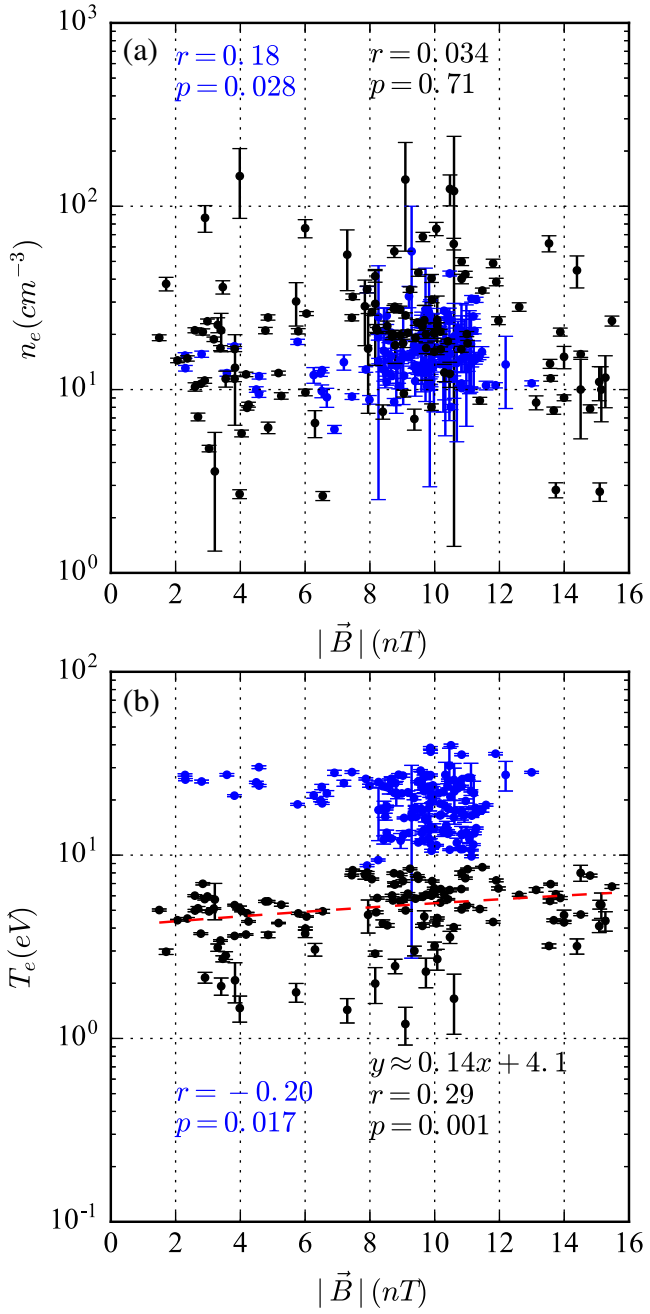

Figure 6. Scatter plots of the warm electron population's density versus magnetic field strength (panel a) and temperature versus magnetic field strength (panel b) over the entire day of 2014 November 1. Measurements with a temperature above and below 8.6 eV are coloured blue and black, respectively. Linear regression (red dashed line) is performed when the correlation between samples is found to be strongly statistically significant (i.e. $p < 0.01$).

(2) The electron DEF below 100 eV is strongly regulated by the temperature of the warm electron population.

(3) The warm electron population is made up of two sub-populations. These two sub-populations dominate at different times, have different relationships between density and temperature, and are categorized by their temperature relative to 8.6 eV.

(4) The warm electron density is not affected by the local neutral pressure or magnetic field strength.

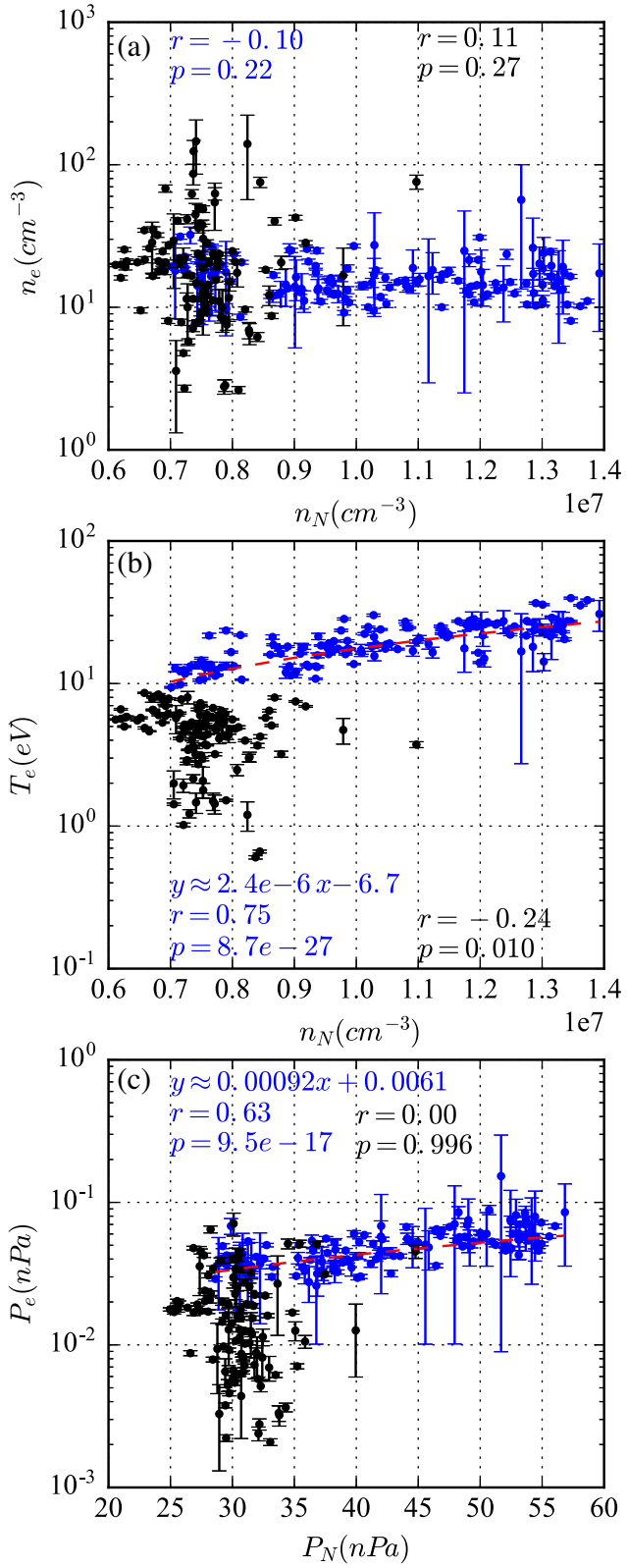

Figure 7. Scatter plots of the warm electron population's density versus neutral density (panel a), temperature versus neutral density (panel b), and electron thermal pressure versus neutral thermal pressure (panel c) over the entire day of 2014 November 1. Measurements with a temperature above and below 8.6 eV are coloured blue and black, respectively. Linear regression (red dashed line) is performed when the correlation between samples is found to be strongly statistically significant (i.e. $p < 0.01$).

Table 2. An estimate of the mean free path of solar wind protons and 20 eV electrons in a water coma based on equation (2) and the observed maximum and minimum neutral densities on 2014 November 1.

Species	n_N (cm^{-3})	σ (cm^2)	λ (km)
Protons	0.7×10^7	2×10^{-15}	710
Electrons	0.7×10^7	5×10^{-16}	2850
Protons	1.5×10^7	2×10^{-15}	330
Electrons	1.5×10^7	5×10^{-16}	1330

(5) The warm electron temperature for sub-population 2 is correlated with the local magnetic field strength.

(6) The warm electron temperature for sub-population 1 is strongly correlated with the local neutral gas density.

Fig. 2 shows that the electron DEF became significantly enhanced, and the solar wind was decelerated before 04:00, between 10:00 and 14:00, and after 17:00 on 2014 November 1. Nilsson et al. (2015b) found that the deceleration and heating of the solar wind occurred when collisions between the solar wind protons and cometary neutrals were significant. The intervals of solar wind proton deceleration and heating seem well correlated with regions of enhanced neutral density shown in Fig. 4(f).

Moment analysis of the IES ion observations shows that the proton density (Fig. 4e, red data) dropped by at least a factor of 2 or 3 during enhanced neutral streams (Fig. 4e). Fuselier et al. (1991) found that solar wind α particles could charge exchange with cometary neutrals to produce He^+, and Burch et al. (2015) further showed that the charge exchange between the solar wind protons and the coma could produce a negatively charged solar wind. The process discussed by Burch et al. (2015) requires the solar wind protons to gain two electrons through charge exchange. Consequently, we consider it very likely that a substantial portion of the solar wind protons are converted into neutral hydrogen while simultaneously producing a heavy population of cometary ions with zero velocity in the rest frame. It is unclear why we do not observe an increase in the cometary ion density as the solar wind proton density decreases, or why the densities are so much lower than the electrons. However, we speculate that this could be caused by the highly directional nature of cometary pickup ions and this direction may be out of the IES's field of view. In equation (2), the mean free path of ions and electrons, λ, is estimated from the local neutral density, n_N, and the cross-section for electron-neutral and ion-neutral collisions, σ.

$$\lambda = \frac{1}{n_N \times \sigma}. \quad (2)$$

On 2014 November 1, the local neutral density varied between $\sim 0.7 \times 10^7$ and $\sim 1.5 \times 10^7$ cm^{-3} because of the local heterogeneity in 67P's coma (Hässig et al. 2015). The cross-section for 20 eV electrons to transfer momentum with water is $\sim 5 \times 10^{-16}$ cm^2, and is smaller for electrons at higher energies (Itikawa & Mason 2005). The cross-section for solar wind ions with cometary neutrals is estimated to be between 2×10^{-15} and 3.5×10^{-15} cm^2 (Mendis et al. 1986; Mandt et al. 2016); we will assume 2×10^{-15} cm^2 for our calculations. The cross-section for charge exchange between solar wind protons and cometary neutrals is also estimated at 2×10^{-15} cm^2 (Burch et al. 2015). Table 2 estimates the mean free path of solar wind protons and 20 eV electrons based on the neutral pressure extrema on 2014 November 1. Rubin et al. (2014) modelled 67P's coma at 2.7 au and found its scale size to be only a few hundred kilometres. Consequently, it seems likely that the observed solar wind deceleration in Fig. 2 was caused by momentum transfer and charge exchange with dense neutral streamers. However, the electrons in the same regions have sufficiently long mean free paths to remain effectively collisionless in 67P's small coma.

Fig. 4(b) shows that electron DEF below 100 eV is affected by the temperature of the warm electron population. Intervals with the highest DEF correspond to temperatures up to 43 eV. Moreover, the density of the warm electron population seems to be largely constant throughout the day. Broiles et al. (2016) noted a similar result when looking at IES electron observations on a separate day. Periodic increases in the intensity of electrons below 100 eV were common before 2015 February (Clark et al. 2015; Broiles et al. 2016).

The relationship between warm electron density and temperature in Fig. 5 suggests that the warm electron population has at least two sub-populations. Warm electrons above 8.6 eV (sub-population 1) cool much faster as density increases. This may indicate that the two populations have different origins or that they experience different heating or cooling mechanisms.

Figs 6(a) and 7(a), respectively, show that there is no relationship between the warm electron density and the magnetic field strength or the local neutral density. The lack of correlation between the warm electron density and the magnetic field strength suggests that the warm electrons are not solar wind electrons convected into the coma and compressed with the local interplanetary magnetic field. Similarly, the lack of correlation between the warm electron density and local neutral density suggests that the warm electrons are not significantly populated by cometary photoelectrons. Edberg et al. (2015) found that LAP and MIP measurements of cometary electrons were well correlated with the local neutral density, which seems contradictory to our results. However, LAP and MIP measure electrons at all energies, while the IES can measure only electrons between 4.3 and 18 000 keV. Broiles et al. (2016) speculated that the cometary photoelectrons were quickly cooled to a temperature below 4.3 eV and were unlikely to be observed by the IES without a spacecraft potential greater than $\sim$4 V.

Results from Fig. 6(b) indicate that the temperature of sub-population 2 is correlated with the local magnetic field strength. We suggest that the warm electrons with temperatures below 8.6 eV were created elsewhere in the coma and experienced perpendicular heating during transport with the compression of field lines draped in the coma. This was hypothesized by Nemeth et al. (2017).

Fig. 7(b) shows that the temperature of sub-population 1 is strongly correlated with the local neutral density. Galand et al. (2017) found a similar positive correlation between electron DEF below 100 eV and neutral density, but found that it only occurred in the winter hemisphere of the coma. Nevertheless, a positive correlation between electron temperature and neutral density directly conflicts with observations from previous missions, which determined that electrons cool as the neutral density increases due to higher collision rates (Bame et al. 1986; Zwickl et al. 1986; Gan & Cravens 1990). Table 2 suggests that the cometary electrons on 2014 November 1 had a sufficiently long mean free path to not experience significant cooling. Simultaneously, the solar wind protons and newly formed cometary ions have a relatively short mean free path, which will produce counterstreaming ion populations. The flow of ion populations relative to each other produces free energy, which will lead to instabilities such as the lower hybrid wave (Gary 1993; Shapiro et al. 1999; Clark et al. 2015).

Unfortunately, burst-mode observations were not available from LAP on 2014 November 1, which prevents a direct comparison between electrostatic wave observations and results shown previously.

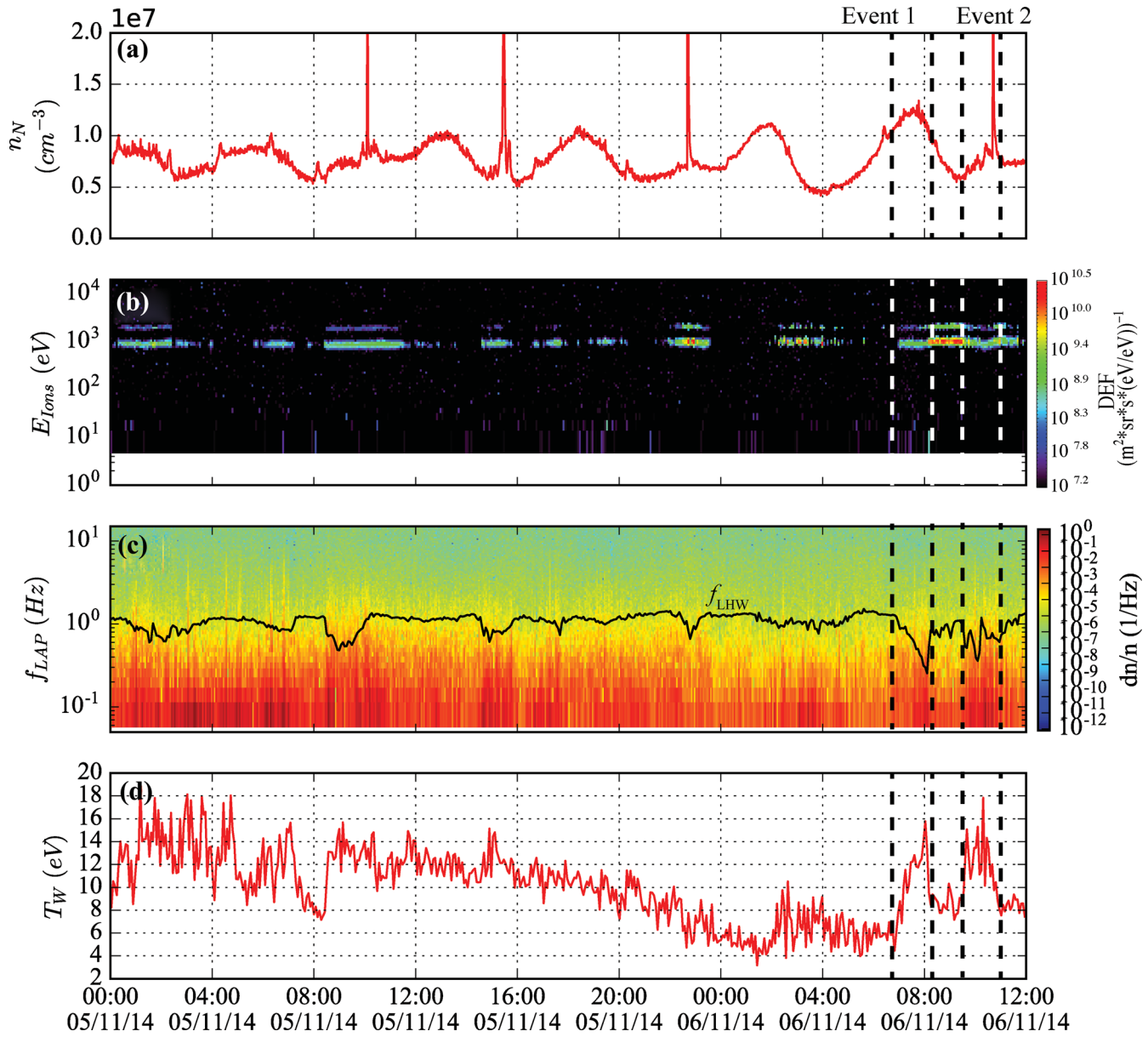

Figure 8. A time-series analysis of COPS, LAP, and IES observations from 00:00 2014 November 5 to 12:00 2014 November 6, Panel (a): COPS neutral density; panel (b): IES DEF for ions at each energy step over time; panel (c): power spectral density measured by LAP; and panel (d): warm electron temperature computed from our fitting results. The black curve in panel (c) is the computed lower hybrid frequency, f_{LHW}. Vertical dashed lines near 07:00 and 10:00 on November 6 highlight two events of interest.

However, LAP did make burst-mode observations from 00:00 2015 November 5 to 12:00 2015 November 6, as shown in Fig. 8. From the top to bottom, Fig. 8 shows the COPS neutral density, the IES DEF for ions at each energy step over time, the LAP power spectral density (PSD), and the warm electron temperature computed from fitting analysis. The LAP PSD is a measure of the change in current divided by the average current (i.e. d*I*/*I*), which is a proxy for plasma density oscillations divided by the total density (i.e. d*n*/*n*). We have highlighted two intervals of interest near 07:00 (Event 1) and 10:00 (Event 2) on November 6. The 6h periodic enhancements in neutral density are the same as those described by Hässig et al. (2015), and are more pronounced on this day relative to our previously discussed observations. We note four spikes in neutral density, which are caused by spacecraft slews and are similar to the spikes shown in Fig. 4(g). Wave activity below 1 Hz appears to be nearly continuous, but we note slight enhancements during the neutral pressure peaks. The solar wind periodically disappears throughout the day, which we attribute to solar wind deflections out of the IES's field of view (Broiles et al. 2015; Behar et al. 2016).

We have also estimated the frequency of the lower hybrid wave, f_{LHW}, during this interval in Fig. 8(c) with equation (3) (Shapiro et al. 1999). The lower hybrid frequency of the waves is computed from the ion plasma frequency, ω_{pi}, the electron plasma frequency, ω_{pe}, and the electron cyclotron frequency, ω_{ce}. Under conditions typical of a comet, the electron plasma frequency dominates over the electron cyclotron frequency, and the equation can be approximated as dependent only on the electron and ion cyclotron frequencies, ω_{ci}. We assume that the ions are singly charged, and, based on the moment analysis shown in Fig. 4(e), the effective ion mass is that of water ions (i.e. 18 amu). These assumptions further reduce the

equation, and make the lower hybrid frequency dependent on the elementary charge, q, the magnetic field strength, $|\boldsymbol{B}|$, the electron mass, m_e, and the ion mass, m_i.

$$f_{\mathrm{LHW}} = \frac{\omega_{\mathrm{pi}}}{2\pi\left(1+\frac{\omega_{\mathrm{pe}}^2}{\omega_{\mathrm{ce}}^2}\right)} \approx \frac{\sqrt{\omega_{\mathrm{ce}}\omega_{\mathrm{ci}}}}{2\pi} = \frac{q\,|\,\boldsymbol{B}\,|}{2\pi\sqrt{m_e m_i}}. \quad (3)$$

During Events 1 and 2, we note moderately enhanced neutral pressures (panel a), which also correspond to a slight slowing of the solar wind protons (panel b). There is also enhanced wave activity during both events. During Event 1, the lower hybrid frequency gradually decreases to 0.2 Hz and then abruptly returns to 1 Hz. The warm electron temperature (panel d) elevated during both events, and in the case of Event 1, it appears to correlate with the dip in lower hybrid frequency. Consequently, it appears very likely that electrostatic waves are being produced by the solar wind interacting with the coma of 67P. Waves with a frequency greater than the lower hybrid frequency are being damped through electron Landau resonance, which simultaneously heats electrons to temperatures above 17.2 eV.

Lower hybrid waves were observed from ground observations of the artificial cometosphere produced by the Active Magnetospheric Particle Tracer Experiment (Bernhardt et al. 1987; Gary 1993). Moreover, theory predicts that lower hybrid waves should occur at comets, and that they should heat cometary electrons parallel to the magnetic field (Shapiro et al. 1999). This hypothesis is further supported in our own results by the large reduced χ^2 values returned by our fitting technique for measurements with hot temperatures (Fig. 4d; our model assumes a scalar temperature, while lower hybrid waves preferentially heat electrons in the parallel direction; Gary 1993). Finally, we note that Zwickl et al. (1986) observed the temperature of the warm electron population to be hottest in the flanks of comet Giacabini–Zinner, where the solar wind might still penetrate the coma.

The newly heated electrons are consequential to much of the coma's physics and chemistry. Electron impact ionization is shown to be a significant driver for the production of cometary ions, particularly in the winter hemisphere of the coma (Galand et al. 2017). Moreover, the heated electrons may significantly affect the chemistry occurring in the coma (Fuselier et al. 2015, 2016). Additionally, warm electron–neutral collisions in the coma may be a source for soft X-ray production (Shapiro et al. 1999).

7 SUMMARY

We find that the warm cometary electron population discussed by Broiles et al. (2016) is made up of two sub-populations, each dominant at different times. Intervals when the warm cometary electron population has temperatures greater than 8.6 eV are dominant in local neutral density compression regions. Intervals when the warm cometary electron population has temperatures below 8.6 eV dominate in local neutral density rarefaction regions. Neither of the sub-populations' densities is well ordered by the local neutral pressure or magnetic field strength, suggesting that they do not originate in the solar wind or from cometary photoelectrons. However, the temperature of the sub-population above 8.6 eV is well correlated by the local neutral density, while the temperature of the sub-population below 8.6 eV is well ordered by the local magnetic field strength. Ultimately, we found it consistent with data that the sub-population above 8.6 eV is being heated by lower hybrid waves driven by the counterstreaming of solar wind protons and cometary ions in collisional, high-density neutral gas streams.

ACKNOWLEDGEMENTS

The work on the IES was supported, in part, by the National Aeronautics and Space Administration through contract #1345493 with the Jet Propulsion Laboratory, California Institute of Technology. We thank the teams at the Imperial College London and ESA who have been responsible for the operation of the IES. The work on RPC-MAG was financially supported by the German Ministerium für Wirtschaft und Energie and the Deutsches Zentrum für Luft- und Raumfahrt under contract 50QP 1401. We acknowledge the staff of CDDP and IC for the use of AMDA and the RPC Quicklook data base (provided by a collaboration between the Centre de Données de la Physique des Plasmas, supported by CNRS, CNES, Observatoire de Paris and Université Paul Sabatier, Toulouse, and Imperial College London, supported by the UK Science and Technology Facilities Council). Work on ROSINA-COPS at the University of Bern was funded by the State of Bern, the Swiss National Science Foundation, and by the ESA PRODEX programme.

REFERENCES

Balsiger H. et al., 2007, Space Sci. Rev., 128, 745
Bame S. J. et al., 1986, Science, 232, 356
Behar E., Nilsson H., Wieser G. S., Nemeth Z., Broiles T. W., Richter I., 2016, Geophys. Res. Lett., 43, 4
Bernhardt P. A., Roussel-Dupre R. A., Pongratz M. B., Haerendel G., Valenzuela A., Gurnett D. A., Anderson R. R., 1987, J. Geophys. Res., 92, 5777
Broiles T. W. et al., 2015, A&A, 583, 7
Broiles T. W. et al., 2016, J. Geophys. Res., 121, 7407
Burch J. L., Goldstein R., Cravens T. E., Gibson W. C., Lundin R. N., Pollock C. J., Winningham J. D., Young D. T., 2007, Space Sci. Rev., 128, 697
Burch J. L., Cravens T. E., Llera K., Goldstein R., Mokashi P., Tzou C.-Y., Broiles T., 2015, Geophys. Res. Lett., 42, 5125
Carr C. et al., 2007, Space Sci. Rev., 128, 629
Clark G. et al., 2015, A&A, 583, 6
Cravens T. E., 1987, Adv. Space Res., 7, 147
Cravens T. E., Kozyra J. U., Nagy A. F., Gombosi T. I., Kurtz M., 1987, J. Geophys. Res., 92, 7341
Edberg N. J. T. et al., 2015, Geophys. Res. Lett., 42, 4263
Eriksson A. I. et al., 2006, Space Sci. Rev., 128, 729
Fuselier S. A., Shelley E. G., Goldstein B. E., Goldstein R., Neugebauer M., Ip W.-H., Balsiger H., Reme H., 1991, ApJ, 379, 734
Fuselier S. A. et al., 2015, A&A, 583
Fuselier S. A. et al., 2016, MNRAS, 462, S67
Galand M. et al., 2017, MNRAS, in press
Gan L., Cravens T. E., 1990, J. Geophys. Res., 95, 6285
Gary S. P., 1993, Theory of Space Plasma Microinstabilities. Cambridge Univ. Press, Cambridge
Glassmeier K.-H. et al., 2007, Space Sci. Rev., 128, 649
Goldstein R. et al., 2015, Geophys. Res. Lett., 42, 3093
Gringauz K. I. et al., 1986, Nature, 321, 282
Hässig M. et al., 2015, Science, 347, aaa0276
Itikawa Y., Mason N., 2005, J. Phys. Chem. Ref. Data, 34, 1
Johnstone A. D., 1990, in Mason J. W., ed., Organization, Plasma, Gas Vol. 1, Comet Halley: Investigations, Results, Interpretations. Prentice-Hall, Englewood Cliffs, NJ, p. 57
Larson D. E., Anderson K. A., Lin R. P., Carlson C. W., Réme H., Glassmeier K. H., Neubauer F. M., 1992, J. Geophys. Res., 97, 2907
Livadiotis G., McComas D. J., 2013, Space Sci. Rev., 175, 183
Mandt K. E. et al., 2016, MNRAS, 462, S9
Mendis D. A., Smith E. J., Tsurutani B. T., Slavin J. A., Jones D. E., Siscoe G. L., 1986, Geophys. Res. Lett., 13, 239
Nemeth Z. et al., 2017, MNRAS, in press

Nilsson H. et al., 2007, Space Sci. Rev., 128, 671
Nilsson H. et al., 2015a, Science, 347, aaa0571
Nilsson H. et al., 2015b, A&A, 583, 8
Nordholt J. E. et al., 2003, Geophys. Res. Lett., 30, 1465
Odelstad E. et al., 2015, Geophys. Res. Lett., 42, 10126
Reme H. et al., 1993, J. Geophys. Res., 98, 20965
Richter I. et al., 2015, Ann. Geophys., 33, 1031
Rubin M. et al., 2014, ApJ, 781, 86
Shapiro V. D., Bingham R., Dawson J. M., Dobe Z., Kellett B. J., Mendis D. A., 1999, J. Geophys. Res., 104, 2537
Thomsen M. F., Bame S. J., Feldman W. C., Gosling J. T., McComas D. J., Young D. T., 1986, J. Geophys. Res., 13, 393
Trotignon J. G. et al., 2006, Space Sci. Rev., 128, 713
Young D. et al., 2004, Icarus, 167, 80
Zwickl R. D., Baker D. N., Bame S. J., Feldman W. C., Fuselier S. A., Huebner W. F., McComas D. J., Young D. T., 1986, Geophys. Res. Lett., 13, 4

This paper has been typeset from a TEX/LATEX file prepared by the author.